## Power-Efficient Autonomous Mobile Robots

Liangkai Liu\*, Weisong Shi<sup>†</sup>, and Kang G. Shin\*
\*Department of Computer Science and Engineering, University of Michigan, USA
<sup>†</sup>Department of Computer and Information Sciences, University of Delaware, USA

Abstract—This paper presents pNav, a novel powersystem that significantly enhances power/energy-efficiency of Autonomous Mobile Robots (AMRs) by jointly optimizing their physical/mechanical and cyber subsystems. By profiling AMRs' power consumption, we identify three challenges in achieving CPS (cyber-physical system) power-efficiency that involve both cyber (C) and physical (P) subsystems: (1) variabilities of system power consumption breakdown, (2) environment-aware navigation locality, and (3) coordination of C and P subsystems. pNav takes a multifaceted approach to achieve power-efficiency of AMRs. First, it integrates millisecond-level power consumption prediction for both C and P subsystems. Second, it includes novel real-time modeling and monitoring of spatial and temporal navigation localities for AMRs. Third, it supports dynamic coordination of AMR software (navigation, detection) and hardware (motors, DVFS driver) configurations. pNav is prototyped using the Robot Operating System (ROS) Navigation Stack, 2D LiDAR, and camera. Our in-depth evaluation with a real robot and Gazebo environments demonstrates a >96% accuracy in predicting power consumption and a 38.1% reduction in power consumption without compromising navigation accuracy and

*Index Terms*—power efficiency, autonomous mobile robotics, cyber-physical systems

#### I. INTRODUCTION

Autonomous mobile robots (AMRs) have been omnipresent, including factories for manufacturing goods and hospitals for food/drug delivery, personal assistance, search & rescue, deep space exploration, etc. [1], [2], [3], [4]. As a prototypical cyber-physical system (CPS), an AMR is composed of the physical (P) subsystem (sensors, motors, batteries, etc.) and the cyber (C) subsystem (computing and communication HW/SW, navigation algorithm/software) [5]. One of the key challenges for AMRs is their power-efficiency. The operation of an AMR is constrained by its limited battery capacity, making its power-efficiency critically important.

The state-of-the-art (SOTA) research on enhancing AMR power-efficiency has taken two main avenues [6], [7]. The first involves energy-efficient motion planning, optimizing the power usage by physical components, and modeling the relationship between motor speed and power consumption [8], [9], [10], [11], [12], [13], [14], [15], [16], [17]. However, the increasing use of GPUs in cyber/embedded systems makes it challenging to meet growing power demands [18]. The second centers around creating energy-efficient cyber/embedded systems, employing Dynamic Voltage and Frequency Scaling (DVFS) [19], [20], [21], [22], [23]. However, these strategies are better suited for mobile electronic devices and may not meet the specific timing constraints of AMRs. Approaches like E2M [24] aim to optimize computing power in AMRs

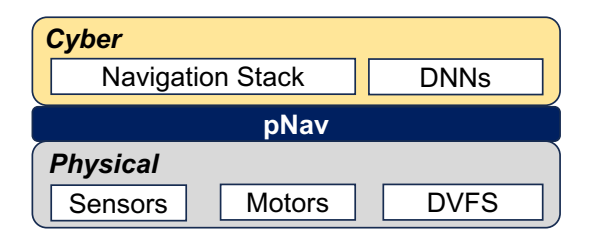


Fig. 1: pNav— holistic power-management system

but often overlook the power consumption by the mechanical/physical subsystem. Another proposal is an end-to-end (e2e) energy model for AMRs [25], but its simple path planning falls short and lacks full system integration. Thus, the central challenge in developing AMRs lies in the optimization of power consumption for *both* cyber (C) and the physical (P) subsystems. To the best of our knowledge, this paper is the first to cover both in-depth.

Joint optimization of C and P subsystems' power consumption requires comprehensive power profiling of AMRs. Therefore, we first developed a representative robot called Donkey and a simulation environment for a detailed analysis of AMR's total power consumption. We then identified three technical challenges in achieving power-efficiency for AMRs. First, there is a lack of understanding of power-breakdown variabilities under different operation speeds and modes. An efficient power-management system needs to model real-time power consumption of both C and P subsystems. Second, ignoring environment-aware navigation localities leads to power wastage. AMRs exhibit significant spatial and temporal localities, i.e., their positions and sensing data are similar over short periods and small spatial areas. Third, uncoordinated C and P subsystems lead to power wastage. Information from the P subsystem, such as the AMR's speed, can help reduce the C subsystem's power consumption, and vice versa. An optimal solution requires the proper co-design of C and P subsystems.

We tackle the above-identified challenges by developing pNav, a holistic power-management system that optimizes the power-efficiency and navigation-safety of AMRs with dynamic and real-time cooridnation of C and P subsystems. as shown in Fig. 1. pNav comprises four key components: Power Predictor, Locality Checker, Collision Predictor, and Coordinator. The Power Predictor (§IV-C) estimates the overall power consumption of an AMR at millisecond-level based on motor speed, CPU/GPU frequencies, and navigation configurations. The prediction model is integrated into the AMR's path planning for navigation. The Locality Checker (§IV-D) focuses on modeling spatial and temporal navigation localities at three

level: data level (robot's Field of View (FOV) overlap), postion level (SLAM particle confidence), and path level (trajectory waypoints). Utilizing LiDAR data, the Collision Predictor (§IV-E) forecasts potential collisions through timeline analysis for the worst-case scenario. It continually assesses the dynamic environment to define a safe time interval, enabling safe adjustments to the navigation configurations of the AMR. Central to pNav is the Coordinator (§IV-F), which integrates the results from various modules to decide whether to run the AMR in the power-saving or performance mode. In power-saving mode, the Coordinator dynamically adjusts motor speed, navigation configurations, and DVFS settings to achieve optimal powerefficiency while considering the updated navigation locality and TTC (Time-To-Collision) constraints. When the navigation locality or TTC falls below a certain threshold, the Coordinator switches to the performance mode to enhance navigation performance. Once the locality and TTC values get higher, the system returns to the power-saving mode. pNav effectively balances power-efficiency and navigation safety for AMRs.

We have prototyped pNav with general/common AMRs hardware (2D LiDAR, camera) and software (ROS navigation stack, detector) designs [26], [27], [16], [28], [29]. Then, we have conducted extensive experiments to assess pNav's effectiveness in terms of the prediction and reduction of power consumption as well as the efficiency of AMR navigation. Our evaluation has shown pNav to achieve an accuracy of over 96% in e2e power-consumption prediction for AMRs. It also reduces power consumption by 38.1% over the baseline AMR configurations. The increase in task execution latency for pNav remains under 6%, making a minimal impact on operational speed. Moreover, the accuracy drop in localization was <2%, showcasing its high navigation precision. pNav also improves AMR's safety by extending the time-to-collision (TTC), thus letting AMRs buy time to react to and avoid potential hazards. Overall, pNav significantly enhances the power-efficiency and navigational safety of AMRs.

This paper makes the following three main contributions:

- A comprehensive and fine-grained power profiling of AMRs, revealing three types of challenges in achieving power-efficient AMRs system: (1) variabilities of system power consumption breakdown, (2) environment-aware navigation locality, and (3) coordination of C and P subsystems (§III);
- Development of pNav, addressing the above inefficiencies. pNav combines a real-time prediction of power consumption for both C and P subsystems, novel modeling and monitoring of navigation localities, a collision prediction module, and effective coordination of both software and hardware configurations across both C and P subsystems to realize energy-efficient and safe AMRs (§IV);
- Prototyping pNav using the ROS Navigation Stack (§VI), and evaluating its effectiveness via extensive experiments.
   Our results demonstrate that pNav achieves a 96% accuracy in power-consumption prediction and reduces power consumption by 38.1% for AMRs. pNav also ensures efficient and safe navigation with a minimal (< 6%)</li>

increase of task latency and a <2% drop in localization accuracy (§VII).

## II. BACKGROUND AND MOTIVATION

#### A. Autonomous Mobile Robots

Software Pipeline: Fig. 2 depicts a general software pipeline for AMRs [29], [28]. The pipeline starts with sensory inputs from odometry, LiDARs, cameras, etc., to such subsystems as Simultaneous Localization and Mapping (SLAM) for mapping and localization, and an object detector for recognizing obstacles. This sensory input data is processed to create both global and local cost-maps, which are essential for navigation. The core of the pipeline involves global and local planners, which work in tandem to build a route toward a designated goal while accounting for real-time environmental changes. Finally, the controller translates these plans into actionable commands for the robot's actuators — typically DC motors — to perform precise movement and interaction with the environment.

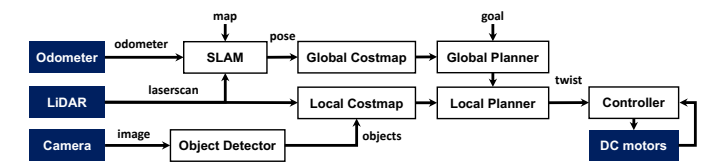


Fig. 2: A general software pipeline for AMRs.

#### B. Motivation

The increasing deployment of AMRs in diverse sectors brings to the forefront the critical need for efficient power management. State-of-the-art (SOTA) approaches to power optimization in AMRs tend to be siloed, focusing on either the planning algorithms or the cyber/embedded systems' efficiency, without a comprehensive, system-wide perspective [10], [11], [12], [13], [14], [15], [24], [25]. This gap calls for an innovative approach that considers the *total* power consumption of each AMR, including sensors, motors, and computing platform, to enhance its endurance and operational effectiveness.

We aim to bridge this gap by developing a comprehensive solution that optimizes power use across all components of AMRs. To the best of our knowledge, this is the first to holistically optimize the power consumption of both the C and P components of AMRs.

# III. CHALLENGES IN ACHIEVING CPS POWER-EFFICIENCY

To understand and identify the technical challenges of power management for AMRs, we have conducted comprehensive empirical studies using Donkey and Turtlebot. We have måde three key observations: 1) variabilities of system power consumption breakdown, 2) environment-dependent navigation localities, 3) coordination of cyber (C) and physical (P) subsystems to achieve optimal power-efficiency.

#### A. Variabilities of System Power Consumption Breakdown

We first break down the power consumption of the end-to-end (e2e) system on a real robot (Section VII). The power-consumption breakdown varies greatly with the motor speed and tasks running on the cyber/embedded subsystem. We choose the four scenarios in Table I to illustrate the power-consumption breakdown. The first three scenarios fix the P part by manually controlling the robot with specific revolutions per minute (RPMs), while the fourth scenario covers the case when the robot is controlled by the navigation stack. For each scenario, we collect the power consumption by each of sensors, motors, and Jetson board. The breakdown of the board's power consumption (CPU, GPU, SOC, etc.) is read from tegrastat.

TABLE I: Four scenarios used for power breakdown.

Scenario	Motor RPM	Control	Navigation Stack	Detection
1	1000	Manual	-	-
2	1000	Manual	<b>✓</b>	<b>✓</b>
3	2000	Manual	<b>√</b>	<b>✓</b>
4	[0, 1000]	Autonomous	<b>√</b>	<b>✓</b>

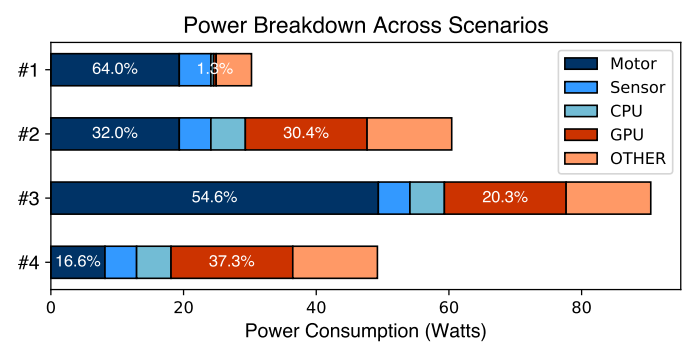


Fig. 3: Power-consumption breakdown.

Fig. 3 shows the breakdown of e2e power consumption in the four scenarios. The robot's total power consumption is found to range from 30W to 90W, while the percentage of the motor's power consumption ranges from 16.6% to 54.6%. The difference between scenario 1 and 2 indicates that robot navigation and object detection consume 30W. Besides, the C subsystem dissipates more power than sensors and motors, whereas the GPU consumes more than 30.4% of the total power. Comparing scenarios 2 and 3 shows that the motor's RPM increases from 1000 to 2000, increasing the motor's power consumption by more than 22%. For scenario 4, the navigation task controls the robot. The motor's RPM is set to be within [0, 1000]. The result for scenario 4 shows that the total power consumption is less than that of scenario 2 because the robot is not always moving. The navigation stack controls the robot to follow the planned trajectories step-by-step to ensure navigation accuracy and safety. Motors are found to consume 16.6% of the total power, while GPU consumes over 37.3%. The variability in power consumption across C and P subsystems corroborates the importance of e2e optimization of power consumption.

**Observation 1:** Power consumption varies with the scenario due to the different underlying control and navigation strate-

gies. Real-time and fine-grained power prediction is, therefore, essential for optimizing e2e power efficiency for AMRs.

#### B. Environment-Dependent Navigation Locality

AMR's Navigation stack tends to process every sensory input from camera and LiDAR equally, which can be computationally expensive and inefficient. In reality, however, not every pixel in each frame is equally important for AMR's navigation. While indoor AMRs are running at low speeds, we observe significant spatial and temporal localities for AMR's navigation. Below we show navigation localities with a timing analysis of sensor data view overlap and linear/angular control of the robot.

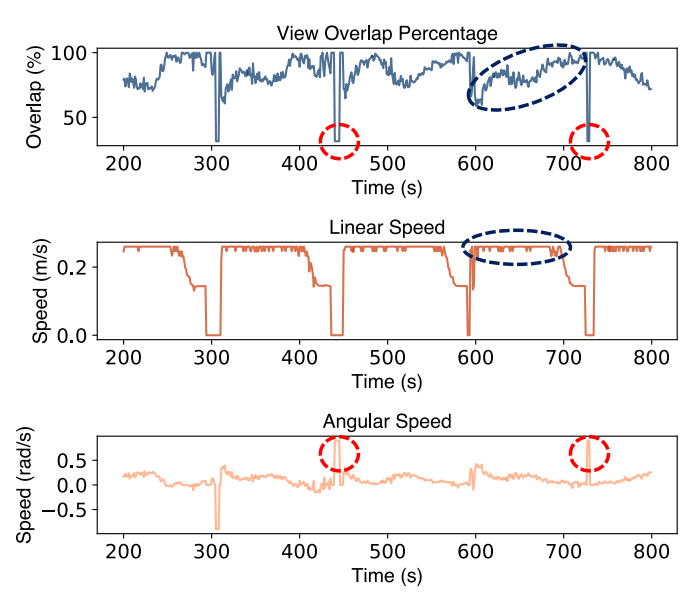


Fig. 4: View overlap with linear/angular speed.

When an AMR is running, two consecutive point clouds or camera frames show a non-negligible similarity. To demonstrate its locality and correlation with the robot's movement, we recorded the sensor readings and calculated the view overlap percentage for two consecutive frames along with the robot's linear and rotational movements/speeds while running the Navigation stack. As illustrated in Fig. 4, for a significant portion of time, the overlap percentage exceeds 80%. Moreover, there exists a noticeable link between movement speed and overlap percentage. Sharp rotational movements result in substantial decreases in view overlap (marked as red circles), whereas the percentage varies minimally during steady linear motion (marked as blue circle). These findings underscore the substantial spatial and temporal relevance of sensing in the AMR's operation, especially when it avoids sharp rotational movements. This observation suggests the dynamic adjustment of AMR operations, such as ROS navigation and object detection, to save energy by leveraging environment-dependent navigation localities.

**Observation 2:** The AMR often operates at low speeds, enhancing both temporal and spatial localities. By exploiting these localities via dynamic adjustments of the navigation stack, a significant improvement of power-efficiency can be made.

#### C. Coordination of C and P Subsystems

According to the AMR's modular design, its C and P subsystems operate independently of each other for environment perception and robot control. This design lacks the coordination of C and P subsystems necessary to achieve optimal power-efficiency. To address this deficiency, we begin with a timing analysis to uncover the causes of power-inefficiency. Fig. 5 shows the power consumption timeline for the AMR's computer, sensors, and motors.

For the C subsystem (computer and sensor), we observe that power consumption spikes to a high level when detection starts and remains high until the detection task ends. In contrast, the motors exhibit more variations in power consumption. When the navigation kicks off, power consumption remains at a low level and increases when the robot starts moving. The motor first accelerates to its highest speed, then maintains this speed, and finally decelerates to stop. When the robot stops, both navigation and detection cease, leading to a noticeable decrease in power consumption for both C and P subsystems.

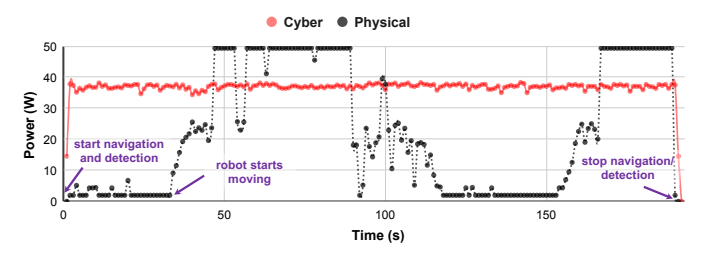


Fig. 5: Power timeline for AMR.

This timeline clearly shows the uncoordinated management of the two subsystems results in significant power wastage. First, even when the robot is not moving, the C subsystem continues to run at high power because it is responsible for environment perception while running navigation and detection tasks at a fixed frequency. If the C subsystem were aware of the robot's control state from the P subsystem, a significant amount of power could have been saved by dynamically changing the opearting frequency for running navigation and detection tasks. Fig. 6 shows the effect of task frequency and motor controls on power cnosumption. The C-subsystem's power consumption can be reduced from 36.5W to 26.8W for YOLOv3 inference on Jetson AGX when the task frequency is lowered from 6Hz to 3Hz. Conversely, if the perception results were shared with and used by the P subsystem, a more power-efficient control trajectory could have been identified and executed (see in §IV-C3), saving a considerable amount of power for the P subsystem. For example, reducing angular speed from 1.2 to 0.4 rad/s reduces power consumption from 92.1W to 19.4W.

**Observation 3:** Uncoordinated C and P subsystems cause substantial power waste. To optimize power-efficiency, C and P subsystems should be jointly designed to achieve optimal power-efficiency.

#### IV. DESIGN OF PNAV

This section presents pNav, which is a power-management system for AMRs. We first provide an overview of the pro-

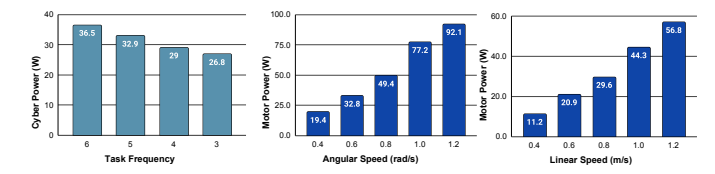


Fig. 6: Impact of Task frequency and motor controls on C/P subsystem's power consumption.

posed system, followed by a discussion of how pNavaddresses the aforementioned technical challenges. Then, we provide the details of pNav's components.

## A. System Overview

Fig. 7 depicts an overview of pNav which is a comprehensive power-management system designed to enhance the energy efficiency and safety of AMRs. It consists of four key components: the Power Predictor, the Locality Checker, the Collision Predictor, and the Coordinator. The Power Predictor estimates the AMR's overall power consumption by analyzing motor RPM commands and feedback, as well as monitoring the current CPU/GPU frequencies. The Locality Checker oversees the navigation locality through monitoring AMCL particle's confidence, camera's FOV overlap, and path planning status. The Collision Predictor utilizes LiDAR data to forecast potential collisions and time-to-collision (TTC), crucial for safe navigation. Central to pNav, the Coordinator synthesizes information from all modules to make informed decisions about CPU and GPU frequencies, and dynamically updates configurations for object detection, costmap, planning, and localization tasks based on TTC and power consumption. This holistic approach positions pNav as an effective solution for managing power consumption while maintaining high safety for AMRs.

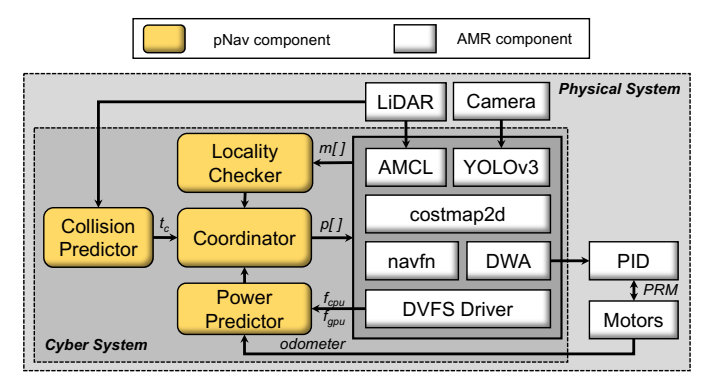


Fig. 7: System architecture of pNav.

#### B. Technical Challenges

pNav addresses several key technical challenges in creating an energy-efficient AMRs system.

C1: Balancing End-to-End (e2e) Power Consumption: This challenge deals with the variation of total power usage of the entire system, including sensors, computing devices, actuators, and other components. pNav tackles this by introducing an e2e power predictor (Section IV-C), which forecasts the power

consumption of the whole AMR system and integrates it into the path planner.

**C2:** Modeling Navigation Locality: Utilizing navigation localities is key to achieving power-efficiency. However, achieving a lightweight and efficient model of navigation localities is non-trivial. pNav addresses this challenge by introducing the Locality Checker which models and monitors the temproal and spatial localities across three leveles: sensor data, robot location, and robot trajectories.

C3: Coordination of C and P Subsystems: Ensuring the safety and efficiency of AMRs in dynamic and unpredictable environments presents significant challenges. pNav tackles these challenges with a centralized Coordinator that continuously adjusts collision prediction and the real-time performance of localization, path planning, and robot control systems. This ensures both power-efficiency and timing/functional predictability.

#### C. Power Predictor

The total power consumption of the AMR  $(P_{\rm AMR})$  is defined as the sum of the total power consumptions of the motors  $(P_{\rm M})$  and the cyber/embedded system  $(P_{\rm ES})$ :

$$P_{\text{AMR}} = P_M + P_{\text{ES}}.$$
 (1)

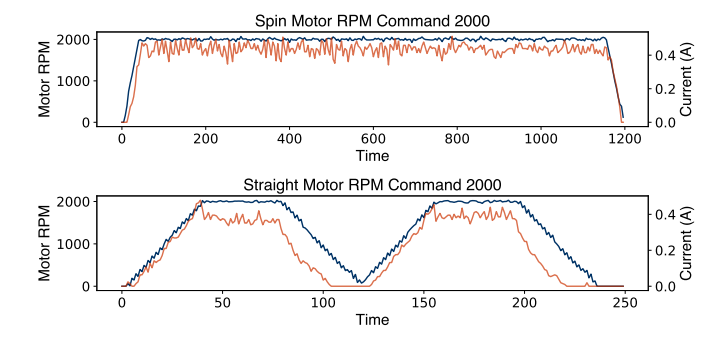


Fig. 8: The timeline for motor's RPM and current.

1) Motor Power Consumption: From the timline in Fig. 8, we can observe a clear relationship between the motor's current and RPM. The power consumption of the motors is given by:

$$P_M = P(v_i, \omega_i, v_{i-1}, \omega_{i-1}), \tag{2}$$

where  $P(v_i, \omega_i, v_{i-1}, \omega_{i-1})$  is the power consumption of the motors at velocities  $v_i$  and  $\omega_i$  and previous velocities  $v_{i-1}$  and  $\omega_{i-1}$ . To predict power consumption, we implement a multi-layer perceptron (MLP). The MLP model uses motor control commands and feedback as input parameters, aiming to predict current in real time at a millisecond level, a significant enhancement over the SOTA that relies on average current at a second level. The models' effectiveness is assessed using Mean Squared Error (MSE) as a loss function to be minimized.

2) Power Consumption by Cyber/Embedded Subsystems: The power consumption of a cyber/embedded system is:

$$P_{\text{ES}} = F_1(f_{\text{cpu}}) + F_2(f_{\text{gpu}}) + F_3(f_{\text{cpu}}, f_{\text{gpu}}),$$
 (3)

where  $P_{\rm ES}$  denotes the system's total power consumption. This equation consists of three primary components.  $F_1(f_{\rm cpu})$  calculates the power consumption by the CPU. The function  $F_1$  depends on the CPU frequency  $f_{\rm cpu}$ .  $F_2(f_{\rm gpu})$  models the GPU's power usage where  $F_2$  is a function of the GPU frequency  $f_{\rm gpu}$ .  $F_3(f_{\rm cpu}, f_{\rm gpu})$  is responsible for calculating the power consumption of other peripherals in the system. The function  $F_3$  is influenced by both CPU and GPU frequencies, capturing the observed behavior that peripheral power consumption jumps when the CPU frequency exceeds 2.0GHz and increases linearly with the GPU frequency.

3) Integration into Path Planner: The path planner is designed for real-time collision avoidance and trajectory generation for mobile robots [30]. It operates by generating a set of velocity commands considering the robot's dynamics, kinematics, and current environmental context. In general, the path planner evaluates these potential commands based on such criteria as collision avoidance, heading toward the goal, and velocity [31].

$$G(\mathbf{v}, \omega) = \sigma(\alpha \cdot \text{heading}(\mathbf{v}, \omega) + \beta \cdot \text{dist}(\mathbf{v}, \omega) + \gamma \cdot \text{vel}(\mathbf{v}, \omega) + \theta \cdot p(\mathbf{v}, \omega)). \tag{4}$$

pNav integrates the power prediction into the cost function of path planner as shown in Eq. (4). The added cost function  $\theta \cdot p(\mathbf{v}, \omega)$  is the predicted motor power consumption given the velocity and rotation for each sample. For all sampled velocity commands, pNav selects the optimal command that maximizes these criteria while ensuring safety.

## D. Locality Checker

To handle a dynamic environment and make the AMR system energy-efficient, we propose a novel approach to model the AMR navigation locality at three levels: data level (robot FOV overlap monitor), position level (particle confidence ratio), and path level (trajectory waypoint monitor).

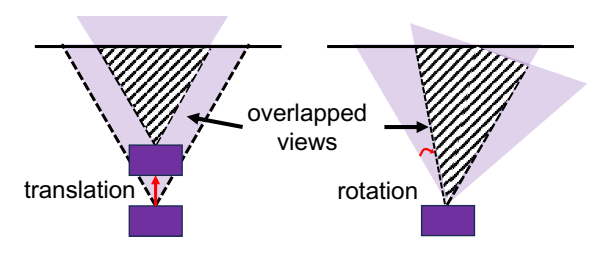


Fig. 9: View overlap when robot is moving.

1) Robot FOV Overlap Monitor: Data similarity in sensing reflects the navigation locality at the data level. The Field of View (FOV) of a camera defines the visible extent of the environment through the camera lens at a particular instance. This angular measurement of the captured scene is crucial in determining the breadth of the environment that can be visualized and recorded. In the context of AMRs, a significant FOV similarity is often observed in consecutive frames, particularly when the AMR is stationary during the planning phase. As a result, the AMR's FOV remains largely unchanged when it is not moving. However, the FOV can vary when the AMR is in motion. Consequently, if a high degree of overlap in

the FOV between successive frames is detected, we prefer the reduction of the frequency of object detection tasks, thus improving power-efficiency.

## Algorithm 1 Calculating Camera FOV Overlap Ratio.

```
1: Input: robot positions p[t_1], p[t_2], robot orientations o[t_1], o[t_2],
      resolution w, h, focal length f_x, f_y
2: Output: FOV overlap ratio \theta
3: function FOVOVERLAP(p[t1], o[t1], p[t2], o[t2], w, h, f_x, f_y)
4: FOV_w \leftarrow 2\arctan\left(\frac{w}{2\cdot f_x}\right), FOV_h \leftarrow 2\arctan\left(\frac{h}{2\cdot f_y}\right) \Rightarrow
Horizontal and Vertical FOV
      Horizontal and Vertical FO
            Fru_{t_1} \leftarrow \mathbf{FOV\_polygon}(p[t_1], o[t_1], FOV_w, FOV_h)
5:
      Frustum intersection at t1
           Fru_{t_2} \leftarrow FOV\_polygon(p[t_2], o[t_2], FOV_w, FOV_h)
6:
      Frustum intersection at t2
 7:
           area_{t_1} \leftarrow Area(Fru_{t_1})
           area_{t_2} \leftarrow Area(Fru_{t_2})
8:
           overlapArea \leftarrow Area(Fru_{t_1} \cap Fru_{t_2}) \triangleright Intersection area
9:
           \theta_{t_2} \leftarrow \frac{overlapArea}{\min(area_{t_1}, area_{t_2})}
10:
            return \theta_{t_2}
12: end function
```

To quantify the similarity between two camera views during robot motion, we introduce an FOV overlap ratio that leverages the camera's intrinsic parameters and the robot's movement. As shown in Fig. 1, the overlap area can vary depending on the robot's translation and rotation. Algorithm 1 outlines the computation steps for the FOV overlap ratio. The process starts by initializing the robot's positions, orientations, and camera parameters (Line 3). The horizontal and vertical FOV angles are computed from the camera intrinsics (Line 4), followed by generation of the FOV polygons (frustums) for the initial and final poses by projecting the camera's view frustum into the environment based on its pose and FOV angles (Lines 5-6). The areas of the individual frustums are then calculated (Lines 7-8), typically using a polygon area function to account for the shape of the projected view. Their intersection area representing the region visible in both camera views—is determined by computing the geometric overlap between the two frustums (Line 9). Finally, the FOV overlap ratio  $\theta$  is computed by normalizing the intersection area with respect to the smaller of the two individual frustum areas (Line 10), providing a scale-invariant measure of visual consistency across the robot's motion.

2) Particle Confidence Ratio: Localization confidence reflects the navigation locality at the position level. This metric is pivotal in gauging the precision and reliability of the robot's localization algorithm [32]. A collection of potential positions, termed particles, are established and dynamically refined based on incoming scan and odometry data. The particle that accumulates the highest scores undergoes clustering to determine the AMR's final position. In this approach, the variation of particles serves as an indicator of the localization algorithm's confidence level. The particles' variations are small when the SLAM system is confident about its localization. We leverage this insight and propose a new metric, called confidence ratio, that involves analysis of the variances of the potential locations (particles). The positions of the particles

are represented in a matrix form, where  $x_i$  and  $y_i$  correspond to the coordinates of each particle:

positions = 
$$\{(x_1, y_1), (x_2, y_2), \dots, (x_n, y_n)\}$$
 (5)

The variance of these positions is then calculated in both the x and y dimensions, capturing dispersion:

variance = 
$$\begin{bmatrix} \operatorname{Var}(x) \\ \operatorname{Var}(y) \end{bmatrix} = \begin{bmatrix} \frac{1}{n} \sum_{i=1}^{n} (x_i - \bar{x})^2 \\ \frac{1}{n} \sum_{i=1}^{n} (y_i - \bar{y})^2 \end{bmatrix}$$
 (6)

Finally, the confidence ratio is computed as the inverse of the sum of these variances, providing a quantifiable metric of localization confidence:

confidence\_ratio = 
$$\frac{1}{\text{Var}(x) + \text{Var}(y)}$$
 (7)

Since particle/hypothesis-based approaches are common in SLAM systems, they offer an effective and correct way to assess the accuracy of SLAM localization. This method is used to monitor the status of SLAM localization and navigation locality.

3) Trajectory Waypoint Monitor: Trajectory waypoints from the path planner reflect the navigation locality at the path level. In general, the path planner periodically generates global and local paths. While the environment can be dynamic and unpredictable, we observe that the waypoints for both local and global paths can be predicted within a certain time window (200ms). This is because the planner usually sets maximum linear and angular speed which constrains AMR's movement within a certain range [29].

Based on this insight, we designed the trajectory waypoint monitor to track the length of both the global and the local plans. The monitor's key functionality lies in its ability to compare the current plan lengths with their previous states. If the global plan's length decreases without the corresponding increase in the local plan's length, it suggests that the robot is successfully moving toward its goal. In contrast, an increase in the global plan's length could indicate a deviation from the intended path or a lack of progress.

Running at a regular interval, the trajectory waypoint monitor continuously invokes its analysis, providing real-time feedback on the robot's path planning efficacy. This continuous monitoring is crucial for quickly identifying potential navigation inefficiencies, thus enhancing the overall performance of AMRs in dynamic environments.

## E. Collision Predictor

The collision predictor is adept at real-time monitoring for potential collisions in dynamic environments and composed of two primary components: the timeline analyzer and the calculation of time to collision (TTC).

1) Timeline Analyzer: The timeline analyzer is responsible for predicting the e2e delays in AMR's tasks. Based on the software pipeline depicted in Fig. 12a, the localization results from SLAM and the detection results from the detector are sent to the local cost-map. This cost-map is then updated and forwarded to the local planner. Finally, the path planner generates local plans and transmits them to the AMR.

Fig. 10 illustrates the timeline of AMR's tasks. The global planner is excluded from this analysis, as it is typically

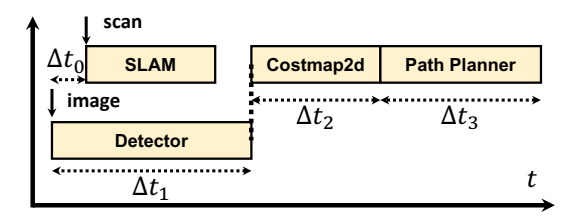


Fig. 10: Timeline analysis of the AMR tasks.

executed once per navigation. Given that the camera and LiDAR operate at different frequencies, there is an initial delay,  $\Delta t_0$ . The delay  $\Delta t_1$  is the maximum of SLAM's or detector's delay, with SLAM's delay  $t_{slam}$  (detector's delay  $t_{object}$ ), depends on CPU (GPU) frequency.  $\Delta t_2$  represents the delay for costmap2d updates, while  $\Delta t_3$  is the delay for the local planner, with both primarily influenced by CPU frequency.

2) Time-to-Collision: The Time-to-Collision (TTC) component of the collision analyzer is designed for the safety of AMRs, utilizing real-time LiDAR data and the robot's current motion. It calculates the time until a potential collision by dividing the shortest distance  $(f_d)$  from the LiDAR scan gives a drivable window  $(V_{max}, W_{max})$ . This approach offers a simple yet effective estimation of the urgency to avoid collisions, ensuring the robot dynamically adapts its path in changing environments. If no obstacle is detected  $(f_d = \infty)$ , the TTC is set to  $\infty$ , indicating a clear path ahead.

$$f_{d} = \min(\operatorname{Scan}(d + v_{i} \cdot t, \theta + \omega_{i} \cdot t))$$
 subject to:  $0 \leq v_{i} \leq V_{\max}, -W_{\max} \leq \omega_{i} \leq W_{\max}$  
$$t_{c} = \begin{cases} \frac{f_{d}}{V_{\max}}, & \text{if } f_{d} \neq \infty \\ \infty, & \text{otherwise} \end{cases}$$
 (9)

To this end, we propose a safe time metric which quantifies the available time before a potential collision by comparing the TTC with the aggregate delays in the robot's operational timeline. This metric is defined as:

$$s_t = t_c - (\Delta t_0 + \Delta t_1 + \Delta t_2 + \Delta t_3),$$
 (10)

where  $t_c$  represents the TTC, determined from the realtime LiDAR data and the robot's velocity. The components  $\Delta t_0, \Delta t_1, \Delta t_2, \Delta t_3$  signify delays associated with the camera and LiDAR data processing, SLAM and detector computations, costmap updates, and local path planning by the path planner, respectively. This metric is scrutinized under two distinct scenarios: the average case, which employs average values of delays, and the extreme case, which accounts for the maximum observed delays. Notably, in extreme cases, these delays can be significantly influenced by the CPU/GPU frequencies, impacting the safe time metric.

## F. Coordinator

The coordinator is designed to collect all profiling information from the power predictor, the navigation checker, and the collision predictor to determine the best system configurations that achieve the lowest total power consumption while guaranteeing the AMR's safety. The system configurations consist of the CPU/GPU frequencies and parameters selection for the navigation stack.

1) CPU/GPU Frequency Optimization for AMRs: A key aspect of enhancing energy efficiency in AMRs involves the strategic selection of CPU and GPU frequencies. This process aims to reduce the overall power consumption  $(P_{ES})$  of the embedded system, while simultaneously ensuring that the TTC  $(t_c)$  is adequately greater than the worst-case sum of all operational delays  $(\Delta t_0 + \Delta t_1 + \Delta t_2 + \Delta t_3)$ . Given that the operational frequency of the camera is 30Hz and the LiDAR is 5Hz, we limit the delay  $t_0$  to a maximum of 33ms. The delay  $t_1$  is dependent on both CPU and GPU frequencies ( $f_{cpu}$  and  $f_{qpu}$ ), while  $t_2$  and  $t_3$  are influenced primarily by  $f_{cpu}$ . Our analysis covers seven distinct CPUs and six GPU frequency levels. By offline profiling, we can identify the worst-case scenarios for each frequency pairing. The optimization problem is thus defined as that of minimizing  $P_{ES}$ , ensuring that the effective TTC remains above a critical threshold  $(t_d)$ :

$$\min P_{\text{ES}}(f_{\text{cpu}}, f_{\text{gpu}}) \text{ s.t. } t_c - (\Delta t_0 + \Delta t_1(f_{\text{cpu}}, f_{\text{gpu}}) + \Delta t_2(f_{\text{cpu}}) + \Delta t_3(f_{\text{cpu}})) \ge t_d$$

$$(11)$$

Considering a small number of possible combinations of CPU and GPU frequencies, the search for the optimal settings are both efficient and computationally economical.

2) Navigation Coordination: With the CPU and GPU frequencies determined and a safe response time  $(s_c)$  established for worst-case scenarios, the coordinator can dynamically toggle the AMR between "power-saving mode" and "recovery mode." This optimization balances performance and safety effectively.

**Power Saving Mode.** Initially, the coordinator assesses results from the Locality Checker to perform a locality test. Specifically, if the FOV overlap ratio and particle confidence fall within predefined thresholds and the path planner demonstrates progress, the AMR enters 'power saving mode.' This mode adjusts the CPU and GPU frequencies to manage the embedded system dynamically. Additionally, the coordinator integrates a power predictor with the path planner (Eq.4) and applies a delay  $(s_t)$  to the detection task, guided by timeline analysis (Eq.10).

**Performance Mode.** If the FOV overlap ratio or particle confidence drops below the set threshold, or if the path planner deviates from its intended path, the AMR switches to 'performance mode.' In this mode, the coordinator adjusts the navigation stack to facilitate recovery. To enhance the FOV overlap ratio, it resets the detection task's delay to zero. To boost particle confidence, it increases the number of particles and the scan beams for the SLAM algorithm. For deviations in path planning, it raises control frequencies and reduces sampling time to refine the trajectory.

## V. DESIGN OF DONKEY, A POWER-PROFILING PLATFORM

To address the challenge of limited comprehensive power profiling in AMRs, we have developed the Donkey powerprofiling platform, an AMR equipped with current sensors on each subsystem (motors, sensors, computing) and specialized

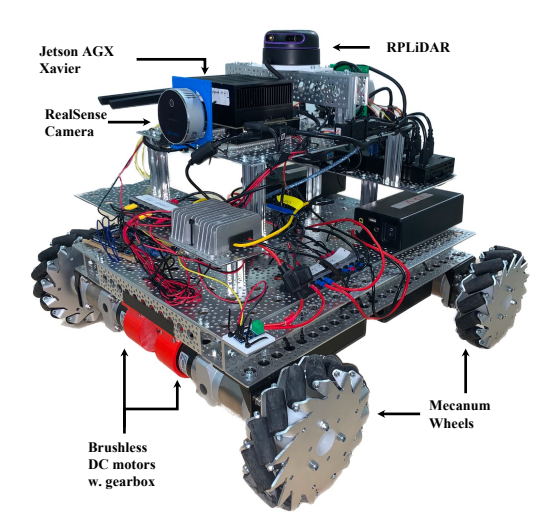


Fig. 11: Donkey platform.

software for power profiling. Below we outline Donkey's hardware, software pipeline, and power monitoring system.

#### A. Hardware Design

For representative power profiling, Donkey is designed and built to follow the general rules [33], [34], [28]. Fig. 11 shows an overview of Donkey which are equipped with four Mecanum wheels. Four brushless DC motors with hall sensor and gearbox are used as the locomotion part. Each motor is controlled by a separate controller using a Pulse-width modulation (PWM) signal on serial communication links. Donkey is also equipped with an Intel RealSense L515 camera and an RPLiDAR A3. Its compute board is an NVIDIA Jetson AGX Xavier. The sensors and motor controllers are connected to the Jetson board through a 10-port USB hub.

## B. Software Pipeline

The autonomous driving software pipeline on Donkey is built with ROS, a middleware framework that supports modular robot development through nodes and topics. The pipeline consists of 4 main stages as shown in Fig. 12a: sensing, perception, planning, and control. Each component is implemented using ROS nodes (individual processes) and topics (communication channels).

Sensing: Donkey uses an RPLiDAR and a RealSense camera for environmental sensing. Sensor data acquisition and publication are handled by dedicated ROS nodes: lidar\_node for the RPLiDAR and camera\_node for the camera. These nodes publish data in standard ROS message formats such as LaserScan and Image. An odometer node estimates the robot's movement using an omniwheel kinematic model.

**Perception:** This stage enables the robot to localize itself and perceive its environment. A map of the indoor environment is first generated using the gmapping package, and localization is performed using Adaptive Monte Carlo Localization (AMCL) which uses odometer and LiDAR's scan to estimate the robot's pose. For dynamic environment perception, Donkey integrates LiDAR and camera data. The yolov3\_detect node

performs object detection on camera images using a pretrained YOLOv3 model. Detected bounding boxes are passed to the <code>Object\_tracking</code> node, which combines them with depth images to track the object's movement. The <code>object\_marker</code> node then transforms the object's position and velocity into the robot's frame and publishes a <code>/people</code> topic for the planning module.

Planning: This stage determines a path from the robot's current location to a target position. Donkey's planning system extends the ROS Navigation Stack to support sensor fusion between LiDAR and camera inputs. It uses a global planner based on Dijkstra's algorithm to compute an overall route on a static costmap, derived from the map server. A local planner, base\_local\_planner, generates motion trajectories using the local costmap, which is continuously updated with dynamic obstacle data including the object's speed and direction.

Control: The control stage translates velocity commands into motor actions. Donkey uses 4 PID controllers to regulate the speed of its brushless DC motors connected to mecanum wheels. Each controller adjusts the motor's RPM based on the difference between the desired and actual speeds, calculated from hall sensor feedback. The control signal is generated by using a weighted sum of proportional, integral, and derivative components, and sent as a /twist message to the motors. This feedback loop ensures stable and desired robot movement in response to planning commands.

#### C. Power Distribution and Monitoring System (PDMS)

Current Sensor-Based Power Monitoring. The Power Distribution and Monitoring System (PDMS) on Donkey enables real-time current monitoring and control across all motors, compute units, and sensors using ACS712 ( $\pm 1.5\%$  error) and INA169 ( $\pm 2\%$  error) sensors, each supporting up to 5A of current [35], [36]. An Arduino Mega 2560 functions as an external ADC, filtering analog signals with  $0.1\mu F$  capacitors and transmitting digitized data to the AGX platform via USB. The Arduino also manages relays to selectively enable or disable power to individual components.

The PDMS supports three core functions: accurate current measurement ( $\pm 2\%$  max error), relay-based power control, and a serial interface for data transmission and control commands. As shown in Fig. 12b, the 24V supply powers the motor controller through an INA169 sensor, while the 12V line feeds two monitored converters: one supplying 5V to a USB hub connected to sensors (RPLiDAR, Intel RealSense L515s, and the Arduino), and another delivering 19.5V to the AGX. All current data are published as real-time ROS messages for system-level monitoring and analysis.

Software-based Power Monitoring. In addition to hardware-based monitoring, the PDMS includes a software-based power monitor using tegrastats to track real-time power usage on the Jetson AGX board. The board features two 3-channel INA3221 monitors for key power rails. One monitor tracks VDD\_GPU, VDD\_CPU, and VDD\_SOC, while the other monitors VDD\_CV, VDDRQ, and SYS5V, with measurement errors under 5%. Tegrastats reports component-level metrics, including current and average power in milliwatts, GPU

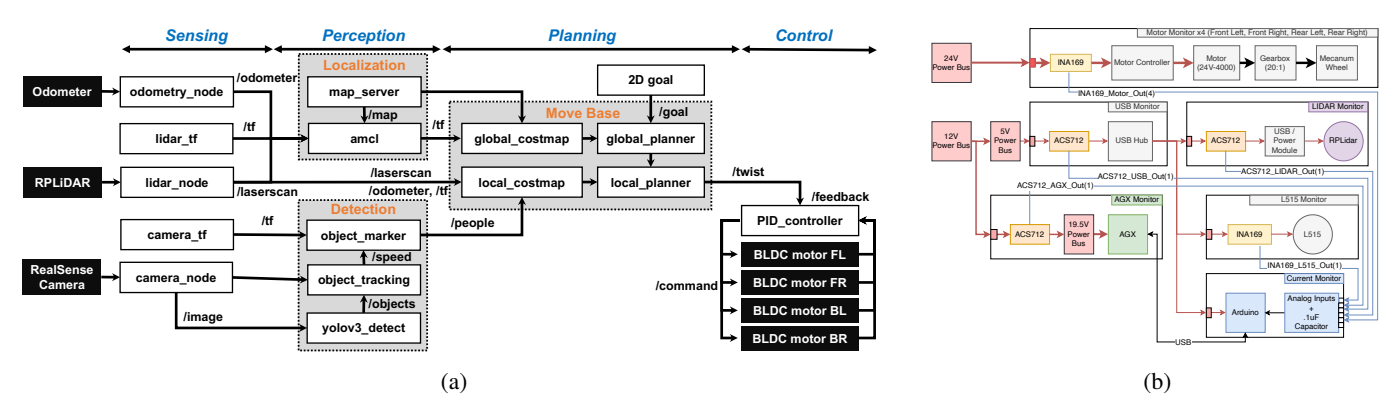


Fig. 12: Overview of (a) Donkey software pipeline and (b) power distribution and monitoring system.

and memory usage (e.g., GR3D\_FREQ for GPU utilization and EMC\_FREQ for memory bandwidth). These readings are integrated into ROS via the ros\_jetson\_stats package, publishing real-time system power data as ROS messages.

[RAM 16496/31760MB SWAP 0/15880MB CPU [19%@2264, 10%@2264, 12%@2264, 16%@2264, 19%@2265, 25%@2265, 25%@2264, 37%@2265] EMC\_FREQ 9%@2133 GR3D\_FREQ 45%@318 GPU 930/930 CPU 2943/2943 SOC 2942/2942 CV 0/0 VDDRQ 774/774 SYS5V 3772/3772]

#### VI. IMPLEMENTATION

To evaluate the performance of pNav, we integrate its implementation into the ROS Navigation stack [29].

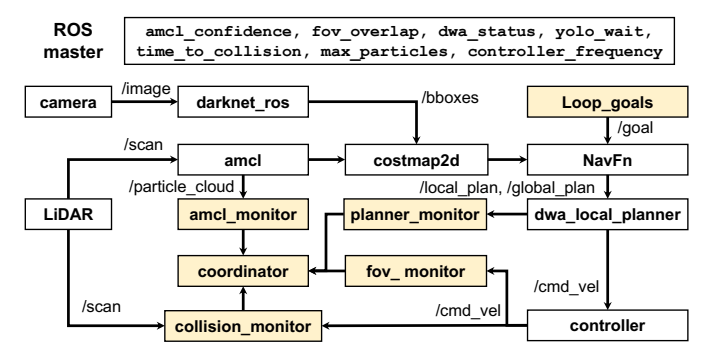


Fig. 13: ROS Implementation of pNav.

ROS Framework. Fig. 13 show a comprehensive ROS framework for pNav. The system integrates multiple components, each dedicated to specific aspects of AMR operations, and is coordinated through ROS. darknet\_ros node runs YOLOv3 for object detection, while dwa\_local\_planner and NavFn nodes are the global and local planners. The key elements of pNav include specialized nodes for AMCL confidence estimation, planner path monitoring, FOV overlap calculation, and a central coordinating node that dynamically adjusts various configurations based on real-time AMR status monitoring.

The amcl\_monitor node continuously assesses the localization accuracy by analyzing the variance of particle clouds, providing a metric of localization reliability. The planner\_monitor observes the lengths of global and

TABLE II: ROS Parameters in pNav.

Name	Type	Range	
amcl_confidence	float	[0.0, ∞]	
fov_overlap	float	[0.0, 1.0)	
dwa_status	boolean	{PLANNING, RUNNING}	
yolo_wait	integer (ms)	[0, 200]	
time_to_collision	float (seconds)	$[0.0, \infty)$	
max_particles	integer	[500, 3000]	
controller_frequency	integer (Hz)	[10, 20, 30]	

local plans generated by the DWA planner, offering insights into the robot's progress towards its goal and its navigational efficiency. The fov monitor node plays a key role in optimizing the operation of vision-based systems like YOLO by determining the overlap between two consecutive frames, allowing for the adjustment of processing frequency to conserve power. Moreover, the colision\_monitor node takes real-time /scan and control messages (/cmd\_vel) and calculate /time\_to\_collision. Central to pNav, the coordinator node orchestrates the system, adjusting the CPU/GPU frequencies and ROS parameters in response to the data received from other nodes. Table II presents the type and range for all the ROS parameters. The coordinator node updates yolo wait to manage YOLOv3's inference frequency. Similarly, it updates controller frequency and max particles to manage amcl and dwa\_local\_planner.

#### VII. EVALUATION

A combination of real-world AMR deployment and Gazebo simulation environments are utilized to evaluate pNav using metrics like power prediction accuracy, power savings, and navigation efficiency. Our key findings are the following:

- pNav is highly accuate in capturing and predicting the e2e power consumption of AMRs. Therefore, it can operate AMRs within an RPM range that not only ensures reliable motor power prediction but also optimizes powerefficiency (§VII-B).
- pNav makes substantial improvements of powerefficiency for AMRs by intelligently adapting frequency settings and navigation configuration according to environmental conditions (§VII-C).
- The design of pNav demonstrates efficient navigation status monitoring, providing not only sufficient and safe nav-

igation but also maintaining operation-efficiency. More importantly, it enhances the safety of AMRs, demonstrating pNav as an efficient navigation tool (§VII-D).

#### A. Experiment Setup

We conduct fine-grained profiling using real robots and a realistic environment simulator. Profiling real AMRs provides a detailed power-consumption breakdown in different testing cases, while profiling with the simulator enables the evaluation of power-efficiency of the software pipeline. Utilizing the Turtlebot model within the Gazebo environment simulator, we simulate a scenario where the Turtlebot Waffle navigates autonomously with the ROS Navigation Stack [29] between designated points, incorporating an object detector based on YOLOv3 to enhance navigation accuracy [37].

**Metrics.** Our evaluation focuses on component-wise latency (including AMCL, Costmap2D, and DWA planner), power consumption across different modules (CPU, GPU, etc.), and localization accuracy, measuring both position and orientation errors defined in Eqs. (12) and (13).  $(x_{\rm est}, y_{\rm est})$  and  $yaw_{\rm est}$  denote the robot's estimated position and orientation by SLAM while  $(x_{\rm gt}, y_{\rm gt})$  and  $yaw_{\rm gt}$  are its real pose.

Position Error = 
$$\sqrt{(x_{\text{est}} - x_{\text{gt}})^2 + (y_{\text{est}} - y_{\text{gt}})^2}$$
 (12)

Orientation Error = 
$$|yaw_{est} - yaw_{gt}|$$
. (13)

A software-based power monitor called tegrastats is leveraged for real-time monitoring of power consumption by different components on the Jetson AGX board. The Jetson AGX Xavier module has two 3-channel INA3221 onboard power monitors for measuring the module's total power consumption. The measurement error of the power monitors is less than 5%. For CPU, GPU, SOC, etc., tegrastats provides current/average power consumption in milliwatts.

**Testing Cases.** To comparatively evaluate pNav, we establish four testing cases that incorporate common cyber and physical energy-saving solutions.

Case #1 (SP): Shortest Path with Default DVFS. For the physical subsystem, both baselines' path planners use the collision-free shortest path, with all other parameters set to their default values as specified in ROS Navigation [28]. For the cyber subsystem, SP uses the default DVFS governors to adjust CPU and GPU frequencies, employing scheutil for CPUs and nvhost\_podgov for GPUs.

Case #2 (SP+uDVFS): Shortest Path with Utilization-Aware DVFS. The physical subsystem is identical to that of Baseline #1. For the cyber subsystem, we design a utilization-aware DVFS governor similar to [20]. Specifically, all available CPU and GPU frequencies are sorted into a list. When the utilization of the CPU or GPU exceeds 80%, the frequency is increased by one step in the list; conversely, if the utilization falls below 30%, the frequency is decreased by one step.

**pNav+uDVFS**: Override the frequency configruation in pNav with the Utilization-Aware DVFS.

We evaluate pNav and the other cases by running the robots for five loops through predefined waypoints.

## B. Prediction of Power Consumption

Our power prediction model forecasts the motor's power consumption through an MLP model while the power consumption of the cyber subsystem is predicted using a linear model. Below we first present the performance of the MLP model for motor's power prediction and then the performance of predicting the AMR's total power consumption.

1) Motor Power Prediction: As illustrated in Fig. 14, our motor power prediction model is shown to yield good accuracy and  $R^2$  values across different RPMs. Specifically, the model's accuracy exceeded 90% in both straight and spinning movements. The  $R^2$  values were consistently above 0.8 for all RPMs during straight movement and exceeded 0.8 for spinning at RPMs of 2000 or higher. Furthermore, one can see a clear linear pattern in the predicted average power with respect to RPM, indicating a direct and predictable relationship between these variables. This linear relationship was more pronounced in the range from 1000 to 3000 RPM, corroborating the effectiveness of our MLP model configuration in capturing and predicting the dynamics of the motor's power consumption.

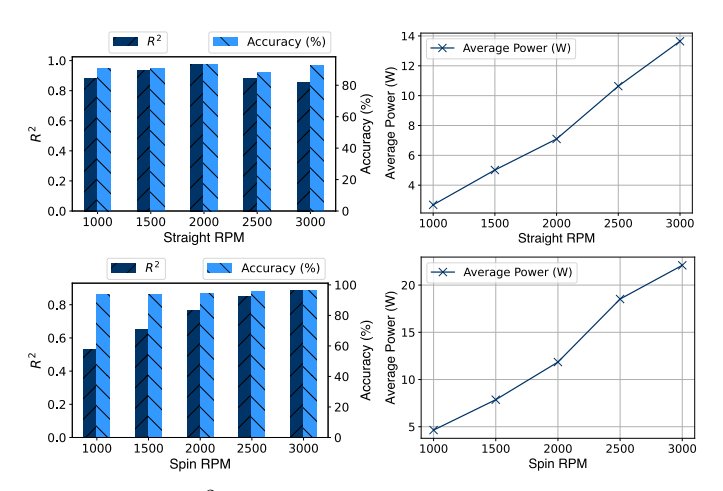


Fig. 14: The  $\mathbb{R}^2$  value and accuracy of the motor power prediction model and the predicted average power under different RPMs.

TABLE III: Average cyber subsystem's power consumption and prediction accuracy at different GPU frequencies.

GPU (MHz)	Predicted Power (W)	Accuracy (%)
420	16.91	99.45
624	18.92	99.31
828	21.53	99.21
1032	24.89	98.80
1198	28.45	98.71
1377	33.38	98.47

2) E2E AMR Power Prediction: For power-sumption prediction for cyber/embedded systems, we initially collected offline power traces to establish a model, as in Eq. (3). From our empirical study, we observed a linear relationship between the power consumption and operating frequencies of CPU and GPU. To validate this model, we configured a Jetson board at various CPU and GPU frequencies and ran our software pipeline, measuring the actual power consumption. The average of both predicted and measured power consumption

was then calculated. The results, as shown in Table III, show that our power prediction model achieves over 98% accuracy across all GPU frequencies.

TABLE IV: E2E power consumption, error, and accuracy for different spin RPMs and straight motion speeds.

Spin RPM	e2e AMR Power (W)	Error (W)	Accuracy (%)
1000	51.96	1.63	96.86
1500	64.82	2.59	96.01
2000	80.76	3.08	96.18
Straight RPM	e2e AMR Power (W)	Error (W)	Accuracy (%)
1000	44.11	1.48	96.64
1500	53.44	2.37	95.56
2000	61.77	2.37	96.15

Using the power consumption predictions for both the motors and the cyber subsystem, we developed a comprehensive e2e power consumption prediction model. Table IV provides the e2e power consumption numbers, along with the error and accuracy numbers, for both spinning and straight-line movements at various RPMs. These results consistently show >95% accuracies across all test cases, corroborating the effectiveness of pNav's power prediction module.

#### C. Power Consumption

To evaluate the effectiveness of pNav in minimizing power consumption, we conducted tests with robots operating under both the baseline configurations and pNav settings, executing identical sets of five goal loops. The power consumption of the cyber subsystem was recorded, and the results are summarized in Table I. This data reveals that pNav significantly reduces power consumption across all components by dynamically adjusting the CPU and GPU frequencies. Notably, the total power consumption was reduced from 60.41W with the testing case SP to 37.38W with pNav, marking a substantial (38.1%) reduction of power consumption. Even comparing with the testing case SP+uDVFS, pNav still reduces over 31% of power.

TABLE V: Power Consumption Comparison.

Power (W)	SP	SP +uDVFS	pNav +uDVFS	pNav	Reduction over SP (%)	Reduction over SP+uDVFS (%)
GPU	15.19	10.3	5.8	2.22	85.41%	78.45%
CPU	8.92	8.6	9.2	7.72	13.41%	10.23%
SOC	5.24	4.7	4.2	3.85	26.58%	18.09%
VDDRQ	2.87	2.6	2	1.66	42.21%	36.15%
SYS5V	4.89	4.7	4.4	4.24	13.36%	9.79%
Motor	23.3	23.3	17.7	17.7	22.5%	24.03%
Total	60.41	54.2	43.3	37.38	38.1%	31.03%

## D. Navigation Efficiency

In addition to the significant reduction of power consumption, pNav is expected to achieve good navigation performance since it monitors the environment and dynamically configures its execution in real time. So, we evaluate the navigation efficiency of pNav in task latency, loop finish time, and navigation safety.

1) Task Latency: Latency is crucial for the efficiency and safety of navigation. Fig. 15 compares the latency boxplot for the AMCL, local costmap, and local planner components between the baseline and pNav. These components are key contributors to the e2e navigation timeline of AMRs. Our

analysis reveals that pNav maintains a similar average latency and distribution to the baseline.

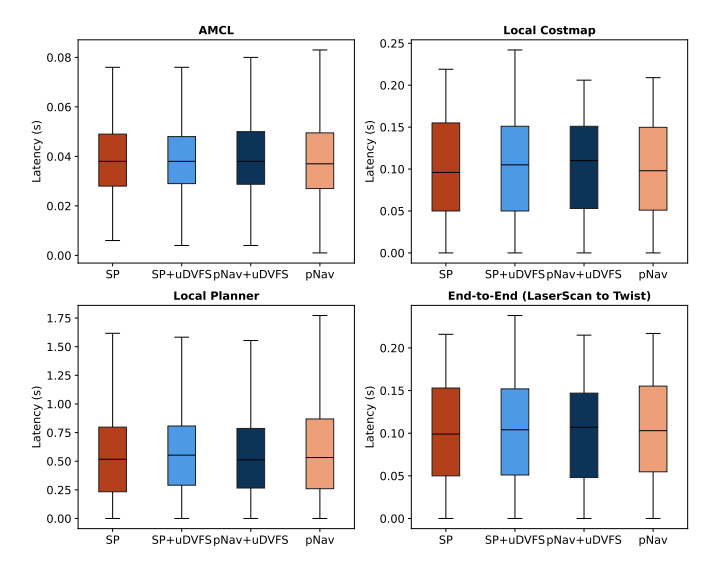


Fig. 15: Boxplot of navigation task latency for the baseline and pNav.

Further insights into the average latency and its changes are provided in Table VI. pNav alters the average e2e latency by a maximum of 1.75%, equivalent to approximately 2ms. This marginal change is negligible in the AMR's safe control.

TABLE VI: Average latency (in milliseconds) for each component across different testing cases.

Latency (ms)	SP	SP +uDVFS	pNav +uDVFS	pNav	% Change over SP
AMCL	40.608	39.154	40.638	38.470	-5.16%
Local Costmap	101.043	101.094	104.016	99.300	-1.72%
Local Planner	565.647	604.053	573.911	628.375	+11.03%
End-to-End	101.420	102.134	100.746	103.176	+1.75%

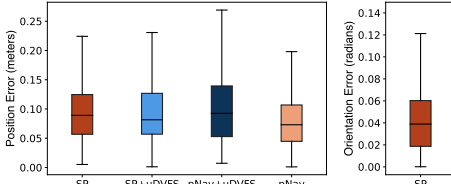
2) Loop Finish Time: The completion time for a loop of goals is critical metric in assessing the operation-efficiency of AMRs. To this end, we collected finish times for 20 goal points under both the baseline and pNav configurations. As shown in Table VII, there are noticeable differences in the average, minimum, and maximum finish times between the two systems. While the baseline exhibits a higher maximum finish time, pNav provides a lower minimum finish time.

TABLE VII: Comparison of Finish Times.

Finish Time (s)	Average	Min	Max
SP	22.64	18.41	25.34
SP+uDVFS	21.92	18.09	33.54
pNav+uDVFS	22.80	17.98	25.92
pNav	20.50	16.47	24.14

Overall, pNav reduces the average finish time by 2.14 seconds (9.4%) compared to the SP case. This improvement demonstrates pNav's navigation efficiency. The increased performance is largely due to pNav's power-efficient planner, which optimizes speed, heading, and distance in a comprehensive manner.

3) Navigation Safety: Our evaluation of navigation safety focuses on two key metrics: localization accuracy and TTC. These metrics are crucial for ensuring the correct localization and adequate reaction time of an AMR. Fig. 16 presents a boxplot comparison of AMCL's positional and orientation errors between all testing cases and pNav. The results show a similar average and distribution of errors for both systems.



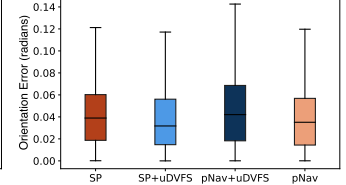


Fig. 16: Boxplot of AMCL accuracy for the baseline and pNav.

Table VIII provides the average positional and orientation errors, along with the percentage changes. pNav demonstrates a 18–38% reduction in error rates compared to the testing case SP. Compared to testing case SP+uDVFS, pNav also reduces 13–50% position and orientation errors.

TABLE VIII: Position and Orientation Errors.

Cases	Position Error (meters)	Orientation Error (radians)	
SP	0.100	0.063	
SP+uDVFS	0.095	0.078	
pNav+uDVFS	0.107	0.103	
pNav	0.082	0.039	
% Change over SP	-18.09	-38.25	
% Change over SP+uDVFS	-13.84	-50.12	

TTC is another crucial safety metric. A longer TTC provides the AMR with more time to react and avoid potential collision. We deployed an additional node to record TTC data at 5Hz for both the baseline and pNav configurations. Table IX summarizes the average, minimum, and maximum TTC. The data reveals that pNav reduces the average TTC by 0.04 second and the minimum TTC by 1.13 second than SP, which is within an acceptable limit for AMR operation. Moreover, pNav extends the maximum time by 0.44 second than SP. This is achieved mainly by integrating power prediction into path selection (Eq. (4)), which reduces the bias for higher speeds.

TABLE IX: Time to Collision.

Cases	Average (s)	Min (s)	Max (s)
SP	6.25	1.84	12.98
SP+uDVFS	6.44	2.61	11.60
pNav+uDVFS	6.22	1.42	13.24
pNav	6.21	0.71	13.42
% Change over SP	-0.04	-1.13	+0.44
% Change over SP+uDVFS	-0.23	-1.9	+1.82

## VIII. RELATED WORK

Various strategies have been proposed to extend the battery life of AMRs. These can be broadly categorized into two main areas: energy-efficient motion planning and optimizing the power-efficiency of embedded systems.

## A. Energy-Efficient Motion Planning

Mechanical components, particularly motors, typically account for about 50% of an AMR's total power consumption. So, considerable research has focused on devising the most energy-efficient paths for robots, either for reaching specific destinations or for area coverage [10], [11], [12], [13], [14], [15]. These studies generally model the correlation between motor speed and power usage, incorporating this model into the robot's navigation algorithms [33], [38]. However, a common limitation of these studies are their predominant focus on the robots' mechanical power consumption, often overlooking or oversimplifying the power demands of computing systems. They become increasingly inaccurate with the growing use of GPUs in embedded systems, which significantly increases power consumption [18].

## B. Power-Efficient Cyber Subsystems

Cyber/embedded systems are pivotal in AMRs as they host all the navigation software. In recent years, numerous studies attempted to optimize the power consumption of embedded systems, particularly using Dynamic Voltage and Frequency Scaling (DVFS) [19], [20], [21], [22], [23]. Some have leveraged application (e.g., games, browsers) profiling combined with DVFS to reduce power consumption in smartphones [19], [21]. Others have concentrated on optimizing the power consumption of Deep Neural Networks (DNNs) running on embedded systems equipped with GPUs [22]. However, these solutions often fall short for AMRs due to their distinct workload characteristics. E2M optimizes the power consumption of embedded systems in AMRs, striking a balance between application performance and minimal power usage of computing resources [24]. However, it largely overlooked the mechanical aspects of AMRs. Another study proposes an e2e energy model for AMRs [25], but it focues on average energy consumption and its path planning is overly simplistic, lacking a fine-grained power management.

pNav provides an orthogonal (hence an alternative) approach to SOTA works on isolated cyber or physical subsystems by co-optimizing both, to achieve better power-efficiency. It extends beyond its initial scope to serve a variety of mobile cyber-physical systems, enhancing tasks from lawn-mowing to managing automated guided vehicles, and even aiding in search & rescue, and battlefield operations.

#### IX. CONCLUSION

We have presented a novel power management system for Autonomous Mobile Robots (AMRs), called pNav. It offers a holistic approach that accounts for the power demands by both the physical and cyber parts of AMRs. Using detailed power profiling of key components and addressing the challenges in balancing e2e power consumption, modeling navigation locality, and coordination of cyber-physical subsystems, pNav not only enhances the AMR's power-efficiency but also ensures the safe and efficient operation of AMRs. The implementation of pNav within the ROS Navigation Stack is shown to reduce the AMR's power consumption by 38.1% and achieved over 96% accuracy in power-consumption prediction. Moreover,

pNav's ability to extend the time-to-collision (TTC) and maintain navigation performance with minimal latency and accuracy impact corroborates its effectiveness in monitoring and controlling modern AMRs.

#### REFERENCES

- [1] R. Siegwart, I. R. Nourbakhsh, and D. Scaramuzza, *Introduction to autonomous mobile robots*. MIT press, 2011.
- [2] D. Avola, G. L. Foresti, L. Cinque, C. Massaroni, G. Vitale, and L. Lombardi, "A multipurpose autonomous robot for target recognition in unknown environments," in 2016 IEEE 14th International Conference on Industrial Informatics (INDIN), July 2016, pp. 766–771.
- [3] H. Durmuş, E. O. Güneş, M. Kırcı, and B. B. Üstündağ, "The design of general purpose autonomous agricultural mobile-robot: "AGROBOT"," in 2015 Fourth International Conference on Agro-Geoinformatics (Agrogeoinformatics), July 2015, pp. 49–53.
- [4] J. Lenchner, C. Isci, J. O. Kephart, C. Mansley, J. Connell, and S. McIntosh, "Towards data center self-diagnosis using a mobile robot," in *Proceedings of the 8th ACM International Conference on Autonomic Computing*, ser. ICAC '11. New York, NY, USA: ACM, 2011, pp. 81–90. [Online]. Available: http://doi.acm.org/10.1145/1998582.1998597
- [5] E. A. Lee, "Cyber physical systems: Design challenges," in 2008 11th IEEE international symposium on object and component-oriented realtime distributed computing (ISORC). IEEE, 2008, pp. 363–369.
- [6] S. Swanborn and I. Malavolta, "Energy efficiency in robotics software: A systematic literature review," in *Proceedings of the 35th IEEE/ACM International Conference on Automated Software Engineering*, 2020, pp. 144–151.
- [7] M. U. Farooq, A. Eizad, and H.-K. Bae, "Power solutions for autonomous mobile robots: A survey," *Robotics and Autonomous Systems*, vol. 159, p. 104285, 2023.
- [8] A. Barili, M. Ceresa, and C. Parisi, "Energy-saving motion control for an autonomous mobile robot," in 1995 Proceedings of the IEEE International Symposium on Industrial Electronics, vol. 2. IEEE, 1995, pp. 674–676.
- [9] Y. Mei, Y.-H. Lu, Y. C. Hu, and C. G. Lee, "A case study of mobile robot's energy consumption and conservation techniques," in *ICAR'05*. *Proceedings.*, 12th International Conference on Advanced Robotics, 2005. IEEE, 2005, pp. 492–497.
- [10] S. Dogru and L. Marques, "Energy efficient coverage path planning for autonomous mobile robots on 3D terrain," in 2015 IEEE International Conference on Autonomous Robot Systems and Competitions, April 2015, pp. 118–123.
- [11] J. A. Broderick, D. M. Tilbury, and E. M. Atkins, "Optimal coverage trajectories for a UGV with tradeoffs for energy and time," *Autonomous Robots*, vol. 36, no. 3, pp. 257–271, Mar 2014. [Online]. Available: https://doi.org/10.1007/s10514-013-9348-x
- [12] C. Henkel, A. Bubeck, and W. Xu, "Energy efficient dynamic window approach for local path planning in mobile service robotics\*\*this work was conducted at the University of Auckland, Auckland, New Zealand," *IFAC-PapersOnLine*, vol. 49, no. 15, pp. 32 – 37, 2016, 9th IFAC Symposium on Intelligent Autonomous Vehicles IAV 2016. [Online]. Available: http://www.sciencedirect.com/science/article/ pii/S2405896316308813
- [13] S. Yu and C. S. G. Lee, "Lifetime maximization in mobile sensor networks with energy harvesting," in 2011 IEEE International Conference on Robotics and Automation, May 2011, pp. 5911–5916.
- [14] C. Anagnostopoulos, S. Hadjiefthymiades, and K. Kolomvatsos, "Accurate, dynamic, and distributed localization of phenomena for mobile sensor networks," ACM Trans. Sen. Netw., vol. 12, no. 2, pp. 9:1–9:59, Apr. 2016. [Online]. Available: http://doi.acm.org/10.1145/ 2882966
- [15] Y. Wang, W. Peng, and Y. Tseng, "Energy-balanced dispatch of mobile sensors in a hybrid wireless sensor network," *IEEE Transactions on Parallel and Distributed Systems*, vol. 21, no. 12, pp. 1836–1850, Dec 2010
- [16] C. Henkel, A. Bubeck, and W. Xu, "Energy efficient dynamic window approach for local path planning in mobile service robotics," *IFAC-papersonline*, vol. 49, no. 15, pp. 32–37, 2016.
- [17] J. Brateman, C. Xian, and Y.-H. Lu, "Energy-effcient scheduling for autonomous mobile robots," in 2006 IFIP international conference on very large scale integration. IEEE, 2006, pp. 361–366.
- [18] "Jetson Modules," 2021, https://developer.nvidia.com/embedded/jetson-modules.

- [19] X. Chen, A. Jindal, N. Ding, Y. C. Hu, M. Gupta, and R. Vannithamby, "Smartphone background activities in the wild: Origin, energy drain, and optimization," in *Proceedings of the 21st Annual International Conference on Mobile Computing and Networking*, 2015, pp. 40–52.
- [20] C. Lin, K. Wang, Z. Li, and Y. Pu, "A workload-aware dvfs robust to concurrent tasks for mobile devices," in *Proceedings of the 29th Annual International Conference on Mobile Computing and Networking*, 2023, pp. 1–16.
- [21] Y. Choi, S. Park, and H. Cha, "Optimizing energy efficiency of browsers in energy-aware scheduling-enabled mobile devices," in *The 25th Annual International Conference on Mobile Computing and Networking*, 2019, pp. 1–16.
- [22] S. Bateni and C. Liu, "neuos: A latency-predictable multi-dimensional optimization framework for dnn-driven autonomous systems," in 2020 USENIX Annual Technical Conference (USENIX ATC 20), 2020, pp. 371–385.
- [23] Y. Choi, S. Park, and H. Cha, "Graphics-aware power governing for mobile devices," in *Proceedings of the 17th annual international conference* on mobile systems, applications, and services, 2019, pp. 469–481.
- [24] L. Liu, J. Chen, M. Brocanelli, and W. Shi, "E2m: an energy-efficient middleware for computer vision applications on autonomous mobile robots," in *Proceedings of the 4th ACM/IEEE Symposium on Edge* Computing, 2019, pp. 59–73.
- [25] L. Liu, R. Zhong, A. Willcock, N. Fisher, and W. Shi, "An open approach to energy-efficient autonomous mobile robots," in 2023 IEEE International Conference on Robotics and Automation (ICRA). IEEE, 2023, pp. 11569–11575.
- [26] S. Gatesichapakorn, J. Takamatsu, and M. Ruchanurucks, "Ros based autonomous mobile robot navigation using 2d lidar and rgb-d camera," in 2019 First international symposium on instrumentation, control, artificial intelligence, and robotics (ICA-SYMP). IEEE, 2019, pp. 151– 154.
- [27] F. d. A. M. Pimentel and P. T. Aquino-Jr, "Evaluation of ros navigation stack for social navigation in simulated environments," *Journal of Intelligent & Robotic Systems*, vol. 102, no. 4, p. 87, 2021.
- [28] "turtlebot3," 2024, https://github.com/ROBOTIS-GIT/turtlebot3.
- [29] "ROS Navigation Stack," 2024, https://github.com/ros-planning/ navigation.
- [30] "dwa\_local\_planner," 2024, http://wiki.ros.org/dwa\\_local\\_planner.
- [31] D. Fox, W. Burgard, and S. Thrun, "The dynamic window approach to collision avoidance," *IEEE Robotics & Automation Magazine*, vol. 4, no. 1, pp. 23–33, 1997.
- [32] "amcl," 2024, http://wiki.ros.org/amcl.
- [33] Y. Mei, Y.-H. Lu, Y. C. Hu, and C. G. Lee, "Energy-efficient motion planning for mobile robots," in *IEEE International Conference on Robotics and Automation*, 2004. Proceedings. ICRA'04. 2004, vol. 5. IEEE, 2004, pp. 4344–4349.
- [34] P. Gaskell, J. Pavlasek, T. Gao, A. Narula, S. Lewis, and O. C. Jenkins, "Mbot: A modular ecosystem for scalable robotics education," in 2024 IEEE International Conference on Robotics and Automation (ICRA). IEEE, 2024, pp. 18 294–18 300.
- [35] Allegro MicroSystems, "ACS712: Hall-Effect-Based Linear Current Sensor IC," Dec. 2021. [Online]. Available: https://www.allegromicro.com/en/products/sense/current-sensor-ics/zero-to-fifty-amp-integrated-conductor-sensor-ics/acs712
- [36] Texas Instruments, "INA1x9 High-Side Measurement Current Shunt Monitor," Dec. 2021. [Online]. Available: https://www.ti.com/lit/ds/ symlink/ina169.pdf
- [37] J. Redmon and A. Farhadi, "YOLOv3: an incremental improvement," arXiv preprint arXiv:1804.02767, 2018.
- [38] S. Liu and D. Sun, "Minimizing energy consumption of wheeled mobile robots via optimal motion planning," *IEEE/ASME Transactions on Mechatronics*, vol. 19, no. 2, pp. 401–411, 2013.